Long range signature of liquid's inertia in nanoscale drainage flows: Supplementary materials

Nathan Bigan[1,2], Mathieu Lizée[1],Marc Pascual[2], Antoine Niguès[1], Lydéric Bocquet[1], Alessandro Siria[1]

[1]Laboratoire de Physique de l'Ecole Normale Supérieure, ENS, Université PSL, CNRS, Sorbonne Université, Université de Paris, 75005 Paris, France
[2]Hummink S.A.S, 5 rue Charlot, 75003 Paris, France

1 Inertial contribution to mechanical impedance

1.1 Geometry and equations

The distance between the sphere and the plane is approximated by a parabolic shape

$$h(r) = h_0 + \frac{1}{2R} r^2 \tag{S1}$$

with R the radius of the sphere.
In the gap, the fluid obeys the Stokes equation of motion, including the inertial term:

$$\rho \frac{\partial v_r}{\partial t} = -\frac{\partial p}{\partial r} + \eta \frac{\partial^2 v_r}{\partial z^2} \tag{S2}$$

as well as the continuity equation

$$\frac{\partial v_z}{\partial z} + \frac{1}{r}\frac{\partial}{\partial r}(r v_r) = 0 \tag{S3}$$

In the lubrication approximation, the pressure field does not depend on z. The variation of the velocity field along z is stronger than along r. One can therefore separate the two different dimensions, r and z. One first solve for the flow along z, and then calculate the pressure along r.

1.2 Flow

The flow is sinusoidal and depends only on z: $v_r(z,t) = v_r(z)e^{j\omega t}$, it thus verifies

$$\eta \frac{\partial^2 v_r(z)}{\partial z^2} - j\omega\rho v_r(z) = \frac{\partial p(r)}{\partial r} \tag{S4}$$

where the pressure field is $p(r,t) = p(r)e^{j\omega t}$.
One introduces the (complex) length scale δ, as

$$\delta^2 = \frac{\nu}{j\omega} \tag{S5}$$

with $\nu = \frac{\eta}{\rho}$ the kinematic viscosity.
The general solution is accordingly

$$v_r(z) = -\frac{\nabla p}{j\omega\rho} + A\cosh\left(\frac{z}{\delta}\right) + B\sinh\left(\frac{z}{\delta}\right) \tag{S6}$$

with $\nabla p = \frac{\partial p}{\partial r}$.
The flow is symetry versus z, so that $B = 0$, and one assumes no-slip boundary condition at $z = \pm\frac{h}{2}$. The solution is accordingly

$$v_r(z) = -\frac{\nabla p}{j\omega\rho}\left[1 - \frac{\cosh\left(\frac{z}{\delta}\right)}{\cosh\left(\frac{h}{2\delta}\right)}\right] \tag{S7}$$

Note that for $\omega \longrightarrow 0$, one indeed recovers the parabolic Poiseuille flow as expected.
The velocity averaged over the vertical gap, $\overline{v}_r = \frac{1}{h}\int_{-h/2}^{h/2} dz v_r(z)$, is accordingly

$$\overline{v} = -\frac{\nabla p}{j\omega\rho} \times \frac{1}{h}\int_{-h/2}^{h/2} dz \left[1 - \frac{\cosh\left(\frac{z}{\delta}\right)}{\cosh\left(\frac{h}{2\delta}\right)}\right] \tag{S8}$$

so that

$$\overline{v}_r = -\frac{\nabla p}{j\omega\rho}\left[1 - \frac{\tanh\left(\frac{h}{2\delta}\right)}{\frac{h}{2\delta}}\right] \tag{S9}$$

1.3 Pressure field

One starts with the continuity equation, S3, which one integrates over z. This yields

$$U - 0 + \frac{1}{r}\frac{\partial}{\partial r}(r h(r)\overline{v}_r) = 0 \tag{S10}$$

where $U(t) = Ue^{j\omega t}$is the imposed vertical velocity of the bead.
One deduces the pressure equation as

$$\frac{1}{r}\frac{\partial}{\partial r}\left(r h(r)\left[1 - \frac{\tanh\left(\frac{h(r)}{2\delta}\right)}{\frac{h(r)}{2\delta}}\right]\frac{\partial p}{\partial r}\right) = j\rho\omega U \tag{S11}$$

A first integration leads to

$$r\left(h(r) - 2\delta\tanh\left[\frac{h(r)}{2\delta}\right]\right)\frac{\partial p}{\partial r} = j\rho\omega U\frac{r^2}{2} + cst \tag{S12}$$

The constant vanishes (cf $r = 0$), yielding

$$\frac{\partial p}{\partial r} = \frac{j\rho\omega U\frac{r}{2}}{h(r) - 2\delta\tanh\left[\frac{h(r)}{2\delta}\right]} \tag{S13}$$

Now,$h(r) = h_0 + \frac{r^2}{2R}$, so that $dh = \frac{r dr}{R}$. One can therefore integrate formally the previous equation as

$$p(r) - 0 = \frac{j\rho\omega UR}{2}\int_h^{"\infty"} \frac{dh}{h - 2\delta\tanh\left[\frac{h}{2\delta}\right]} \tag{S14}$$

Note that we imposed that the oscillating value of the pressure at infinity is vanishing. One concludes that

$$p[h] = \frac{j\rho\omega UR}{2}F\left[\frac{h}{2\delta}\right] \tag{S15}$$

where

$$F(x) = \int_x^{\infty} \frac{dt}{t - \tanh t} \tag{S16}$$

When $\omega \longrightarrow 0$, $\delta \longrightarrow \infty$, then the denominator in the previous integral is $h - 2\delta\tanh\left[\frac{h}{2\delta}\right] \simeq \frac{h^3}{12\delta^2}$, so that one recovers the usual result $p(r) \sim h^{-2}$. However, the integral in S16 does not converge in general, and one should impose an upper bound cutoff, so that one rather writes

$$p[h] = \frac{j\rho\omega UR}{2}\int_{\frac{h}{2\delta}}^{\frac{D_c}{2\delta}} \frac{dt}{t - \tanh t} \tag{S17}$$

The value of the cutoff D_c is to be discussed, see section 1.7.2 below. We argue that it should be $D_c \sim \delta$.
One may introduce

$$F_1(x) = \int_x^{1} \frac{dt}{t - \tanh t} \tag{S18}$$

so that

$$p[h] = \frac{j\rho\omega UR}{2}\left(F_1\left[\frac{h}{2\delta}\right] - F_1\left[\frac{D_c}{2\delta}\right]\right) \tag{S19}$$

1.4 Normal force

The normal (oscillating) force is

$$F_z = -\int_0^\infty \left(-p(r) + 2\eta \frac{\partial v_z}{\partial z}\right) 2\pi r dr \tag{S20}$$

The second term is negligible, so that

$$F_z = -\int_0^\infty -p(r) 2\pi r dr \tag{S21}$$

The change of variables $Rdh = rdr$ allows us to rewrite the integral as

$$F_z = 2\pi R \int_{h_0}^{D_c} p[h] dh \tag{S22}$$

Using the previous result for $p[h]$, one gets

$$F_z = \pi j \rho \omega U R^2 \int_{h_0}^{D_c} dh \left(F_1\left[\frac{h}{2\delta}\right] F_1\left[\frac{D_c}{2\delta}\right]\right) \tag{S23}$$

Since $\delta^2 = \frac{\nu}{j\omega}$, δ is a complex distance, and this shows that F_z has both an imaginary part (the expected case where the force is in phase with the velocity) and a real part .

1.5 Limiting case of high frequency

This corresponds to $2 \mid \delta \mid < h_0$, *i.e.* $\omega > \frac{\nu_0}{h_0^2}$. Note that there are already some frequency (inertial) effects occuring for $\omega > \frac{\nu_0}{R^2}$, due to the previous cutoff issues.
But let's focus here in the above limiting case. In this case, one may approximate $\tanh t \simeq 1$, and

$$p[h] = \frac{j\rho\omega UR}{2} \int_{\frac{h}{2\delta}}^{\frac{D_c}{2\delta}} \frac{dt}{t-1} \simeq \frac{j\rho\omega UR}{2} l \log\left[\frac{h-2\delta}{D_c}\right] \tag{S24}$$

Note that we approximated $D_c - 2\delta \simeq D_\mathrm{c}$ since in this limit $2\delta < h_0 \ll D_\mathrm{c}$.

$$F_z = \pi j \rho \omega U R^2 \int_{h_0}^{D_c} dh \log\left[\frac{h-2\delta}{D_c}\right] \tag{S25}$$

Then

$$F_z = \pi j \rho \omega U R^2 \left(-1 + \frac{h_0 - 2\delta}{D_c} - \frac{h_0 - 2\delta}{D_c} \log\left[\frac{h_0 - 2\delta}{D_c}\right]\right) \tag{S26}$$

We are not interested in this limit.

1.6 Small frequency limit: Reynolds regime

We consider the very small frequency limit, $\omega \longrightarrow 0$. In this case $h/2\delta \longrightarrow 0$.
We approximate $(t - \tanh t)^{-1} \simeq \frac{3}{t^3}$ and insert it in **??**, one gets

$$F(x) \simeq \int_x^\infty dt \frac{3}{t^3} = \frac{3}{2x^2} \tag{S27}$$

Hence, one deduces the Reynolds contribution to the pressure

$$p_R[h] = \frac{3\eta UR}{h^2} \tag{S28}$$

so that,

$$F_z = 2\pi R \int_{h_0}^\infty p[h] dh \tag{S29}$$

and ones recovers the Reynolds formula

$$F_R = 6\pi \frac{\eta U R^2}{h} \tag{S30}$$

1.7 Intermediate frequency regime

1.7.1 Response modulus

We now consider next terms in terms of inertia for the pressure. We write accordingly

$$\frac{1}{t-\tanh t} \simeq \frac{3}{t^3} + \frac{6}{5t} + \mathrm{O}(t) \tag{S31}$$

One gets

$$F(x) \simeq \int_x^{"\infty"} dt \frac{3}{t^3} + \frac{6}{5t} = \frac{3}{2x^2} + \frac{6}{5}\log\left[\frac{x_c}{x}\right] \tag{S32}$$

where we introduce a cutoff x_c in the diverging term, to be discussed below.
Hence,

$$p[h] = p_R(h) + \frac{3j\rho\omega UR}{5}\log\left[\frac{D_c}{h}\right] \tag{S33}$$

The force is again defined as

$$F_z = 2\pi R\int_{h_0}^{\infty} p[h]dh \tag{S34}$$

and one gets

$$F_z[h] = F_R[h] + \frac{6\pi j\rho\omega UR^2}{5}\left(D_c - h + h\log\left[\frac{D_c}{h}\right]\right) \tag{S35}$$

ther real part of this function is the usual Reynolds expression. However, the second term of the force is imaginary and corresponds to the real part of the impedance.
In practice, defining $Z' = -F/a$, with a the displacement, and noting that $U = j\omega a$, then one obtains

$$Z'[h] = \frac{6\pi\rho\omega^2R^2}{5}\left(D_c - h + h\log\left[\frac{D_c}{h}\right]\right) \tag{S36}$$

Note however that this expression is only valid for $h < D_c$, and one expects a vanishing $Z'[h]$ for $h > D_c$.

1.7.2 Cut-off: physical interpretation

The value of the cutoff plays an important role in this problem. When the oscillating bead is far from the wall, *i.e.* $h \gg \delta$, one can imagine that the sphere is surrounded by a fluid sheared layer of thickness $\delta(\omega)$. Beyond this sheared layer, the flow is vanishing. Hence the sphere 'does not see' the wall and one indeed expects a vanishing $Z'[h]$. It is only when the sheared layer 'touches' the wall that the force will be non-vanishing.
Hence this suggests that the cutoff distance should be identified with a length of order δ (and not R as initially thought). Let us write that $D_c = \alpha\sqrt{\nu/\omega}$ with $\alpha = \mathrm{O}(1)$ a numerical factor.
One accordingly predicts the real (elastic) contribution to the mechanical response as

$$\boxed{Z'[h] = \frac{6\pi\rho\omega^2R^2}{5}\left(D_c - h + h\log\left[\frac{D_c}{h}\right]\right)} \tag{S37}$$

with $D_c = \alpha\sqrt{\nu/\omega}$.

1.7.3 Theoretical response considering elasto-hydrodynamic contribution

In this section, we discuss the competition between two effects that govern the elastic response Z': the inertial component and the elasto-hydrodynamic (EHD) response arising from the sample's elasticity. To model the combined effect of these processes, we assume they behave like two parallel springs and sum their respective stiffnesses. The results are depicted in Figures S1,S2 and S3 for 1000 mPa.s, 100 mPa.s and 1 mPa.s silicone oils respectively.

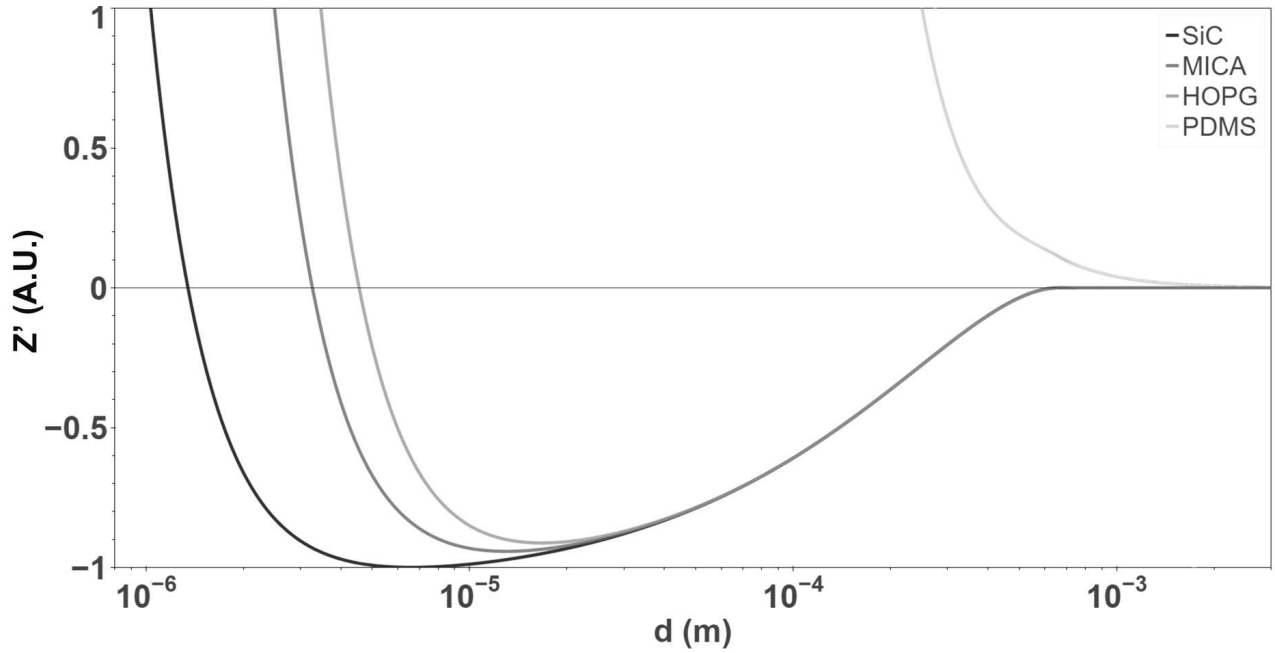

Figure S1: Theoretical normalized Z' (normalized) responses obtained considering both inertial and elasto-hydrodynamic effects for a 1000 mPa.s silicone oil on different substrates.

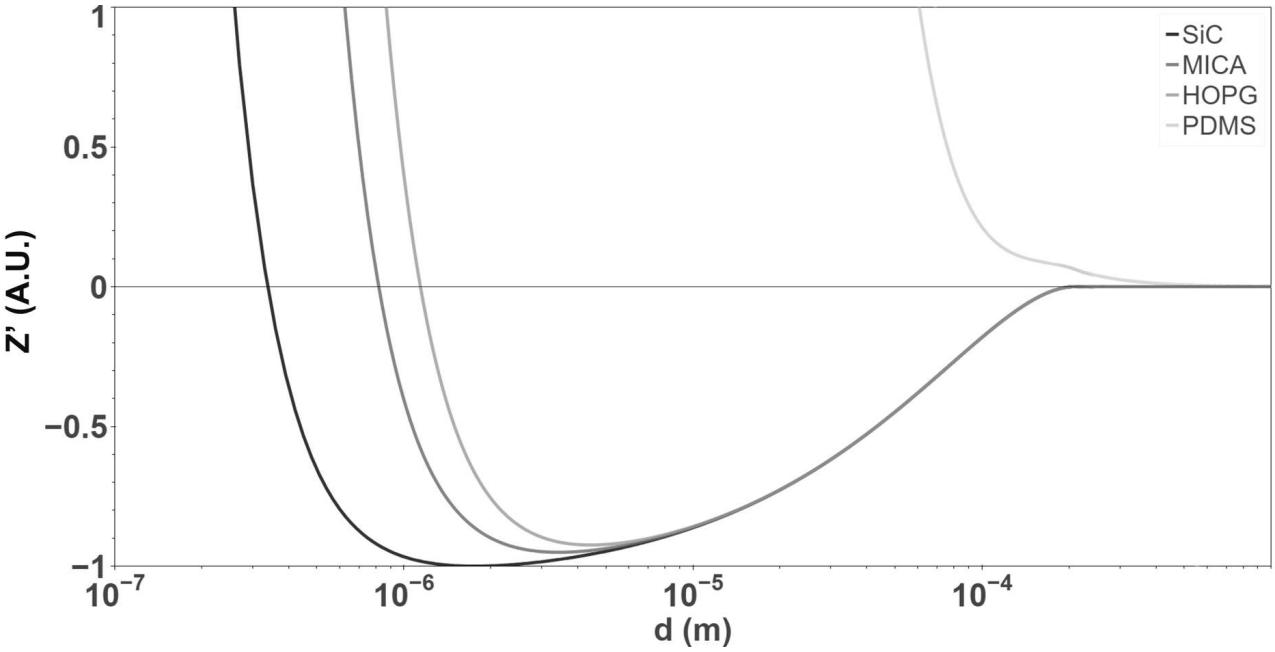

Figure S2: Theoretical normalized Z' responses obtained considering both inertial and elasto-hydrodynamic effects for a 100 mPa.s silicone oil on different substrates.

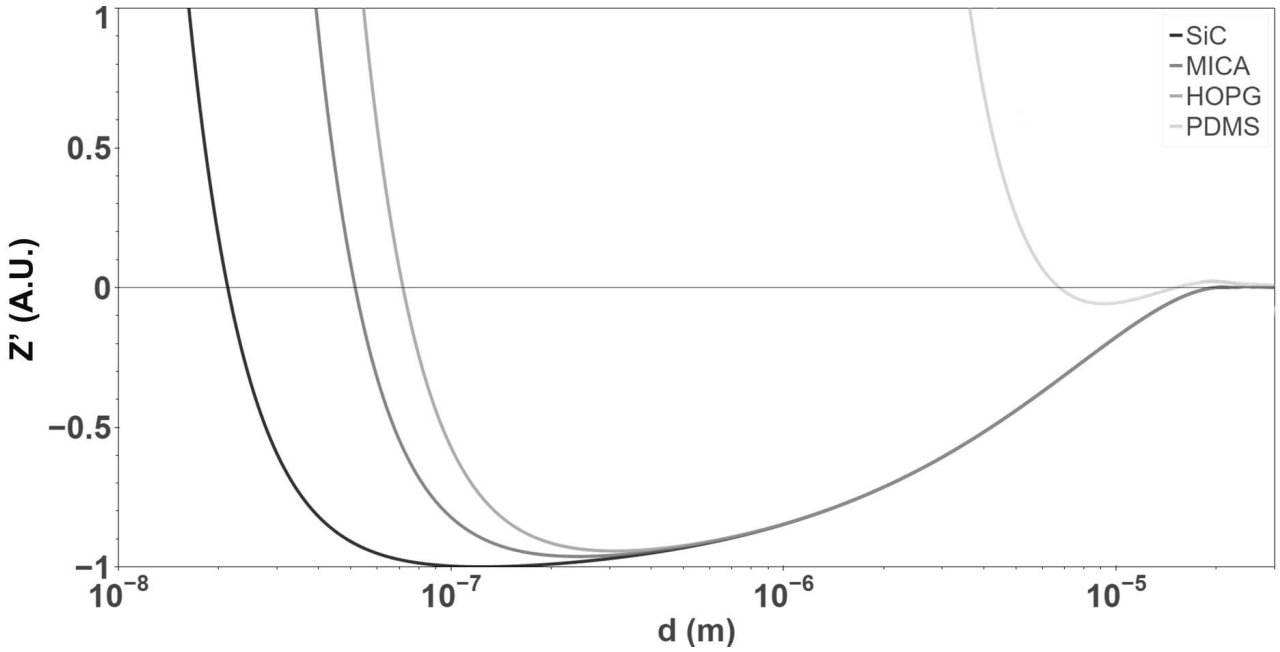

Figure S3: Theoretical normalized Z' (normalized) responses obtained considering both inertial and elasto-hydrodynamic effects for a 1 mPa.s silicone oil on different substrates.

2 Additional Figures

2.1 Tip characterization

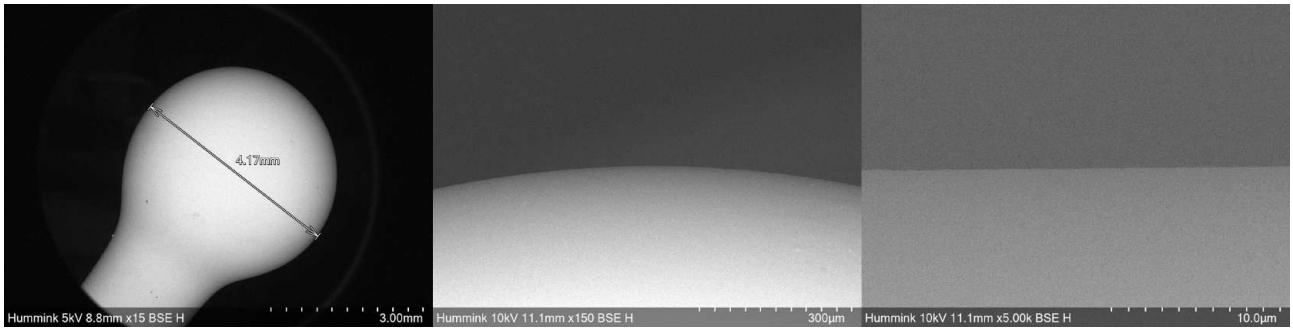

Figure S4: SEM characterization of a typical probe we use in our lab, at three different magnification. These probes are made by fusing a glass rod with an acetylene torch, the surface tension giving them the spherical shape. One can see that at the micro scale, the surface is perfectly flat and particle free.

2.2 Zero determination

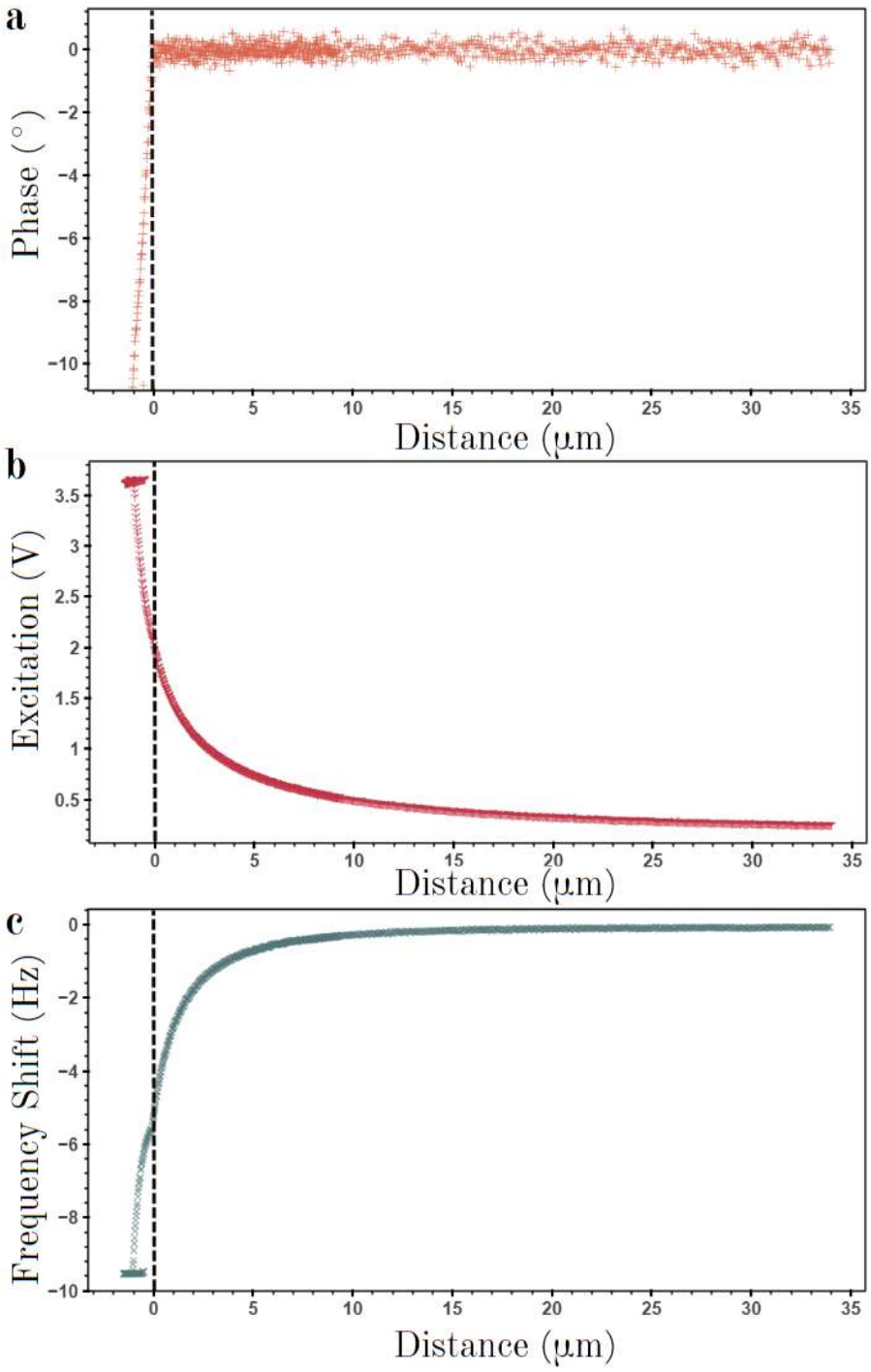

Figure S5: Determination of the solid contact's position.

For each acquisition, the frequency shift, voltage excitation, amplitude, and phase are recorded simultaneously. With the Phase-Locked-Loop active, the phase is typically centered at 0°. A drop-out in the phase indicates a sharp elastic response, which is characteristic of solid contact, allowing us to establish the zero position along the z-axis (dashed line in Figure S5). This method was already introduced in Ref. [1].

2.3 Sphere-plane confinement

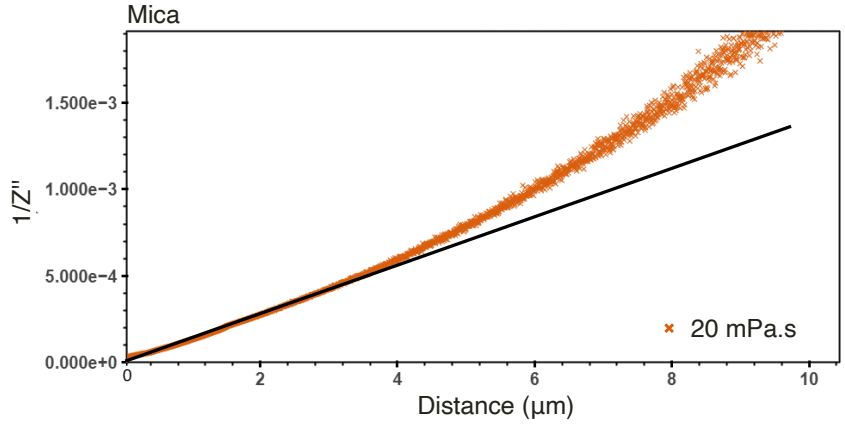

Figure S6: Reynolds scaling of the imaginary part of the impedance Z''

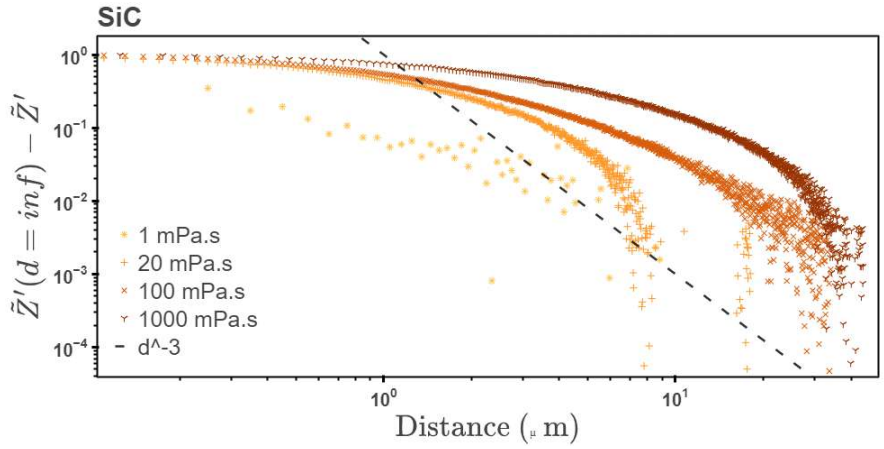

Figure S7: Log-Log plot of the elastic impedance of PDMS on SiC

The dSFA used in this study has a very large millimetric probe and confinement is measured from the far-field down to nanometric length, deep in the lubrication approximation $h \ll R$ and $\delta \ll R$. In consequence, whereas the far-field calculation ($h \gg R$) of Ref.[2] yields a qualitative agreement with experiments from Refs.[3, 4], it is not appropriate for our results in the high confinement regime which are indeed in disagreement with the h^{-3} scaling but rather with a log (see Figure S7).

2.4 Influence of substrate's stiffness

2.4.1 Raw data

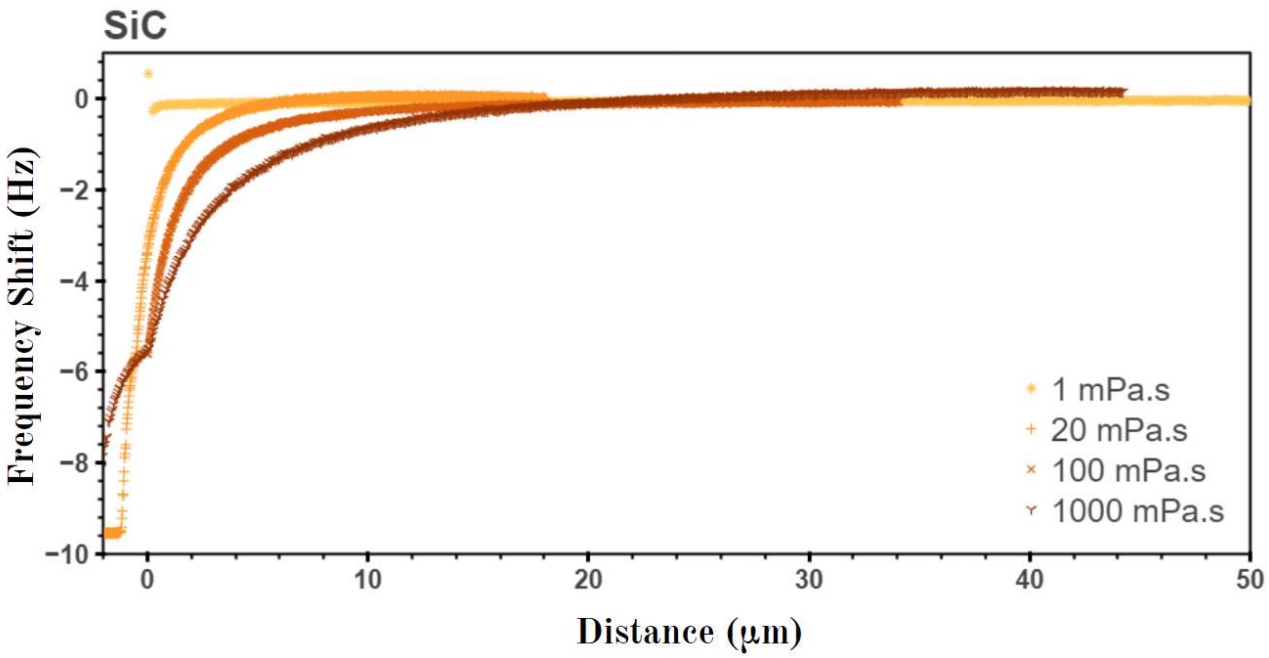

Figure S8: Frequency Shift (Hz) *versus* distance curves for silicon oils on SiC

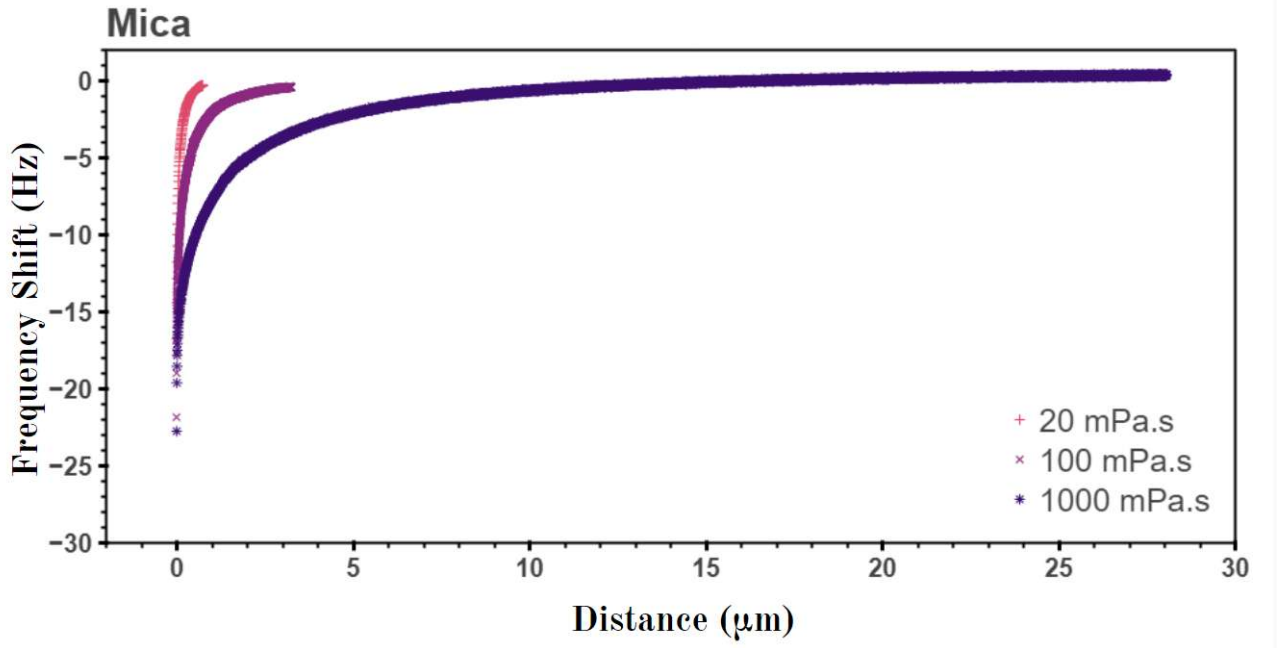

Figure S9: Frequency Shift (Hz) *versus* distance curves for silicon oils on Mica

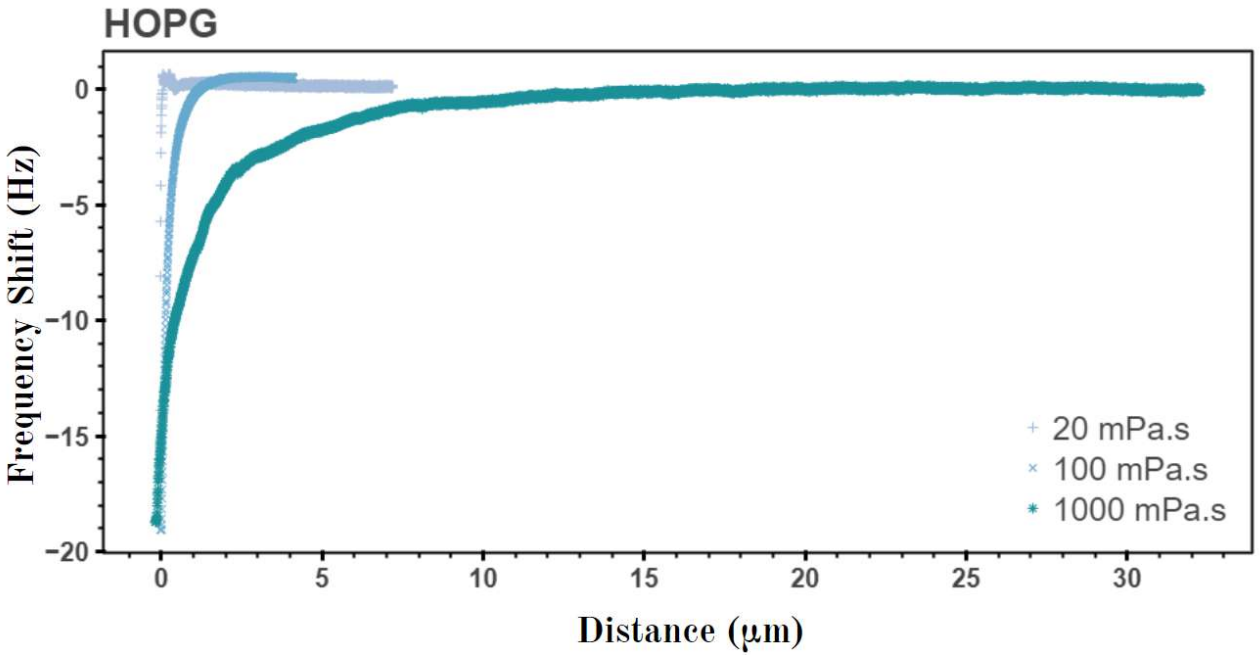

Figure S10: Frequency Shift (Hz) *versus* distance curves for silicon oils on HOPG

2.4.2 Intermediate case

In Figures S1,S2 and S3 we plot the theoretical real mechanical impedance Z' vs distance d for a viscous fluid with viscosity of 1000, 100 and 1 mPa.s (respectively) calculated for all the substrate used during our study.

It can be observed that the inertial effect precedes the elasto-hydrodynamic response by two orders of magnitude for all tested viscosities when using SiC, mica, and HOPG substrates. This explains why we consistently observed a negative frequency shift with all tested liquids under our experimental conditions.
In contrast, for PDMS, the elasto-hydrodynamic length scale, D_{EHD}, is on the same order of magnitude as the inertial length, δ, i.e., $D_{EHD} \sim \delta$. In fact, D_{EHD} is theoretically larger than δ for fluids with viscosities of 100 and 1000 mPa·s, which explains the absence of negative frequency shifts when using PDMS and the corresponding silicone oils.

In the case of less viscous fluids (e.g., 1 mPa·s), the characteristic lengths D_{EHD} and δ are so close that we may observe a competition between the two effects. To verify this hypothesis, we conducted an additional experiment using PDMS as the substrate, with a glass sphere and dioctyl phthalate (viscosity 40 mPa·s) (see Figures S11 and S12).

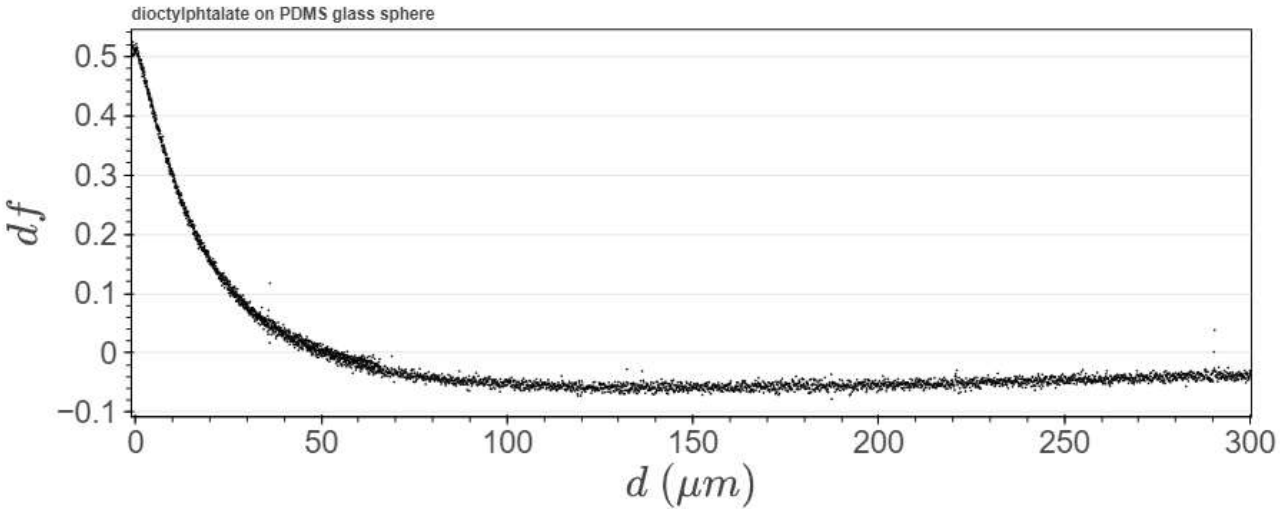

Figure S11: Experimental Frequency shift response obtained with dioctyl phtalate (viscosity ~ 40 mPa.s) confined between the millimetric glasse probe and a PDMS substrate (Young modulus ~ 800 kPa).

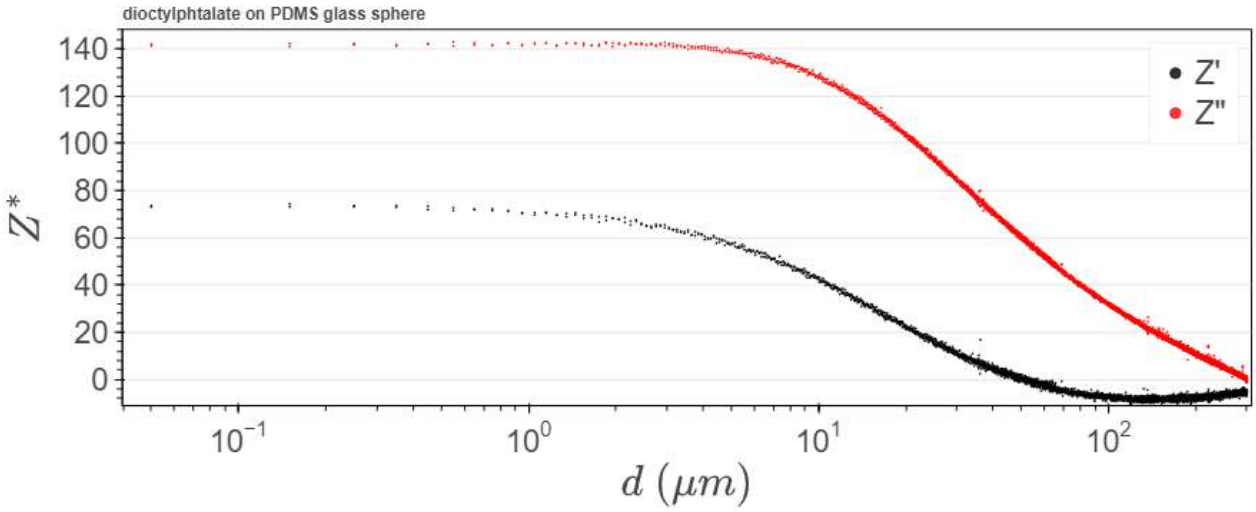

Figure S12: Theoretical Z' responses obtained considering both inertial and elastohydrodynamic effects for a 1 mPa.s silicone oil on different substrates.

In this experiment, we observe the competition between inertial effects and elasto-hydrodynamic responses. At larger distances from the contact point, the inertial effects dominate, leading to a decrease in the frequency shift (and so Z'). However, as the system approaches a critical transition distance (approximately d =100 µm here), the elasto-hydrodynamic response becomes more prominent, causing the frequency shift to increase as the probe approaches the substrate.

2.5 Influence of substrate's rugosity

Until now, we were conducting measurements with smooth surfaces (Mica, SiC and HOPG that have roughness below 1 nm according to literature). Experimentally, we observed that when both the probe and the surface were not perfectly cleaned, dust and visible particles remaining in the contact area systematically prevented us from witnessing the negative frequency shift decay upon approach. We believe that the rugosity induced by the dust particles is of the same order of magnitude than the boundary layer thickness, leading to the detection of the hard contact before the inertial effect.

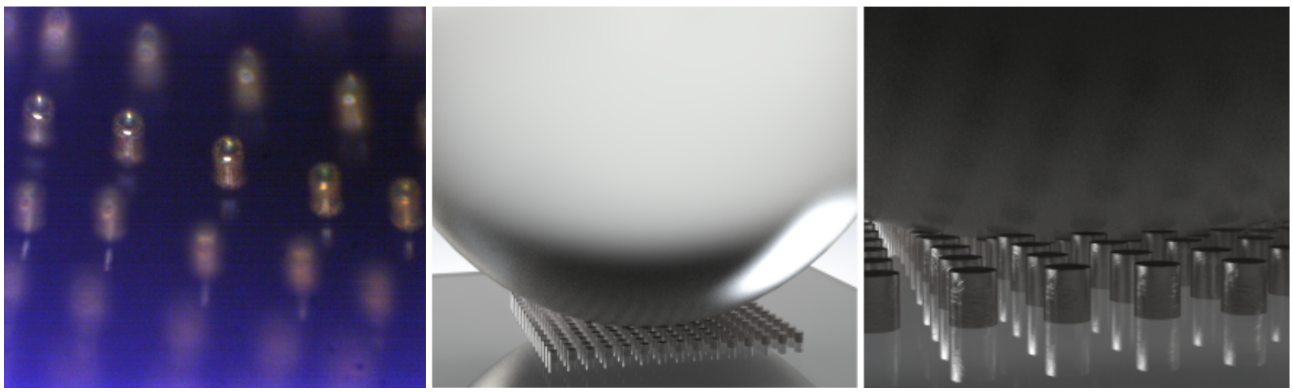

Figure S13: Roughness dependency experiment. Microscope image of the silver pillars array printed with Hummink's patented method (left picture). The pillars have a 4:3 ratio: 30 µm diameter and 40 µm height. Right pictures schematize the approach of the glass sphere compressing the pillars.

In order to verify this theory, we design a sample of controlled roughness by printing micro-pillars with Hummink's Nazca printer [5, 6] on a SiO2 glass slide. These pillars are made of silver nanoparticles thermally sintered, disposed in a 20x20 grid and have a 4:3 size ratio. A drop of AP 1000 Silicon oil (1000 mPa.s) was deposited on the pillar array and the approach was conducted with all other parameters kept similar to previous experiments.

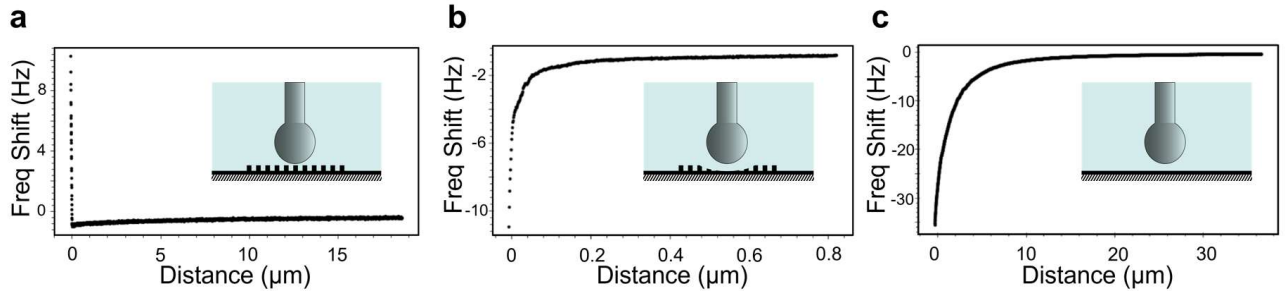

Figure S14: Roughness dependency results obtained with the 1000 mPa.s silicon oil on the silver pillars array. On panel **a** we observe a slow decrease in frequency shift until the hard contact is reached between the glass sphere and the metallic pillars, leading to a typical hertzian contact behaviour. On panel **b** the negative frequency shift is recovered after the compression/detruction of the pillars in the contact zone. Enventually on panel **c** we observe the negative frequency shift obtained for the same oil on the same glass slide without any pillar. Despite the common tendency, the experiment on the clean area of the slide leads to a negative frequency shift decrease at a greater distance away from the solid contact than the destroyed pillars configuration. *NB: Insets are schematic and not at scale.*

We observe in Figure S14 that the confined fluid's response at long distance from the contact (tens of microns) shows the same decrease in frequency shift than those observed with Mica and SiC at similar distances, which was expected as the glass' Young modulus is around 70 GPa. This proves that the porous layer formed by the pillars does not affect much the flow of the inertial boundary layer around the sphere. Nevertheless, as soon as the contact between the pillars tip and the glass sphere is made, the frequency shift rises and we obtain a classical Hertzian contact response, with a linear increase of frequency shift with the distance. The pillars mechanical stiffness induces a hard contact 40 µm away from the glass slide's surface that screens the inertial effect on the frequency shift signal and prevents its complete observation.

To double-check the limited impact of the pillar array on the flow of the inertial boundary layer, we crush the pillars in the contact area between the sphere and the glass slide, then we perform again an approach at the same location. We see on Figure S14**b** that we recover the negative frequency shift behavior, however in a lesser extent than on a clean glass slide like Figure S14**c**: the frequency shift decrease is visible at much longer distances with the clean sample.

We plot in Figure S15 the imaginary part of the mechanical impedance Z" versus the real part Z' (which is equivalent to plotting dissipation versus conservative forces). In this plot the dissipation increases as the confinement distance decreases. We see that for all three configurations (clean surface, surface with pillars array, surface with crushed pillars), the long distance (small Z" values) behavior is the same: a slight frequency shift decrease corresponding to a slight Z' decrease. Then for the pillars array, the hard contact between the pillars and the sphere leads to a positive frequency shift, while the clean surface and the crushed pillars keep on decreasing, although at a different pace. The slope difference between the two suggests that it would be possible to tune the critical distance d_c by changing the surface geometry around the contact area (in particular the pillars' height).
We conclude from these results that while the porous layer formed by the pillars minimally impacts the flow within the inertial boundary layer, it disrupts the liquid's confinement and prevents from sensing the negative Z'. In other words, pillars larger than the penetration length δ prevent the emergence of the inertial effect, whereas pillars smaller than δ reduce the effective inertial effect distance d_c.

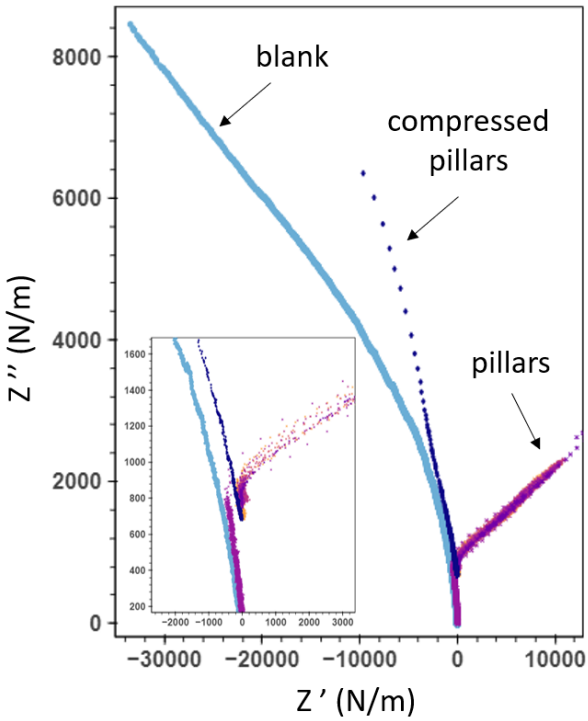

Figure S15: Influence of the substrate's roughness on the mechanical response. All the eight approach and retract experiments conducted on the pillars led to the same characteristic signature, with a slight decrease of the frequency shift at long distances followed by sharp increase upon contact. Both experiments on the clean area and on the crushed pillars give similar behaviors but with different slopes, showing the slight impact of the porous layer on the inertial flow. The zoom-in inset enlightens the similar signature for all systems at long distances.

References

[1] Mathieu Lizée et al. "Anomalous friction of supercooled glycerol on mica". In: *Nature Communications* 15.1 (July 20, 2024). Publisher: Nature Publishing Group, p. 6129. ISSN: 2041-1723. DOI: 10.1038/s41467-024-50232-0.

[2] Itzhak Fouxon and Alexander Leshansky. "Fundamental solution of unsteady Stokes equations and force on an oscillating sphere near a wall". In: *Physical Review E* 98 (Dec. 20, 2018). DOI: 10.1103/PhysRevE.98.063108.

[3] Clémence Devailly et al. "Long-range hydrodynamic forces in liquid FM-AFM". In: *Nanotechnology* 31.45 (Nov. 6, 2020), p. 455501. ISSN: 0957-4484, 1361-6528. DOI: 10.1088/1361-6528/aba786.

[4] Zaicheng Zhang et al. "Unsteady drag force on an immersed sphere oscillating near a wall". In: *Journal of Fluid Mechanics* 977 (Dec. 2023), A21. ISSN: 0022-1120, 1469-7645. DOI: 10.1017/jfm.2023.987.

[5] *HUMMINK - The world's smallest fountain pen revolution*. Hummink. URL: https://hummink.com.

[6] Achille Guitton et al. "Capillary Printing of Fine Structures on Flexible and Hybrid Substrates". In: *2024 IEEE International Conference on Flexible and Printable Sensors and Systems (FLEPS)*. 2024 IEEE International Conference on Flexible and Printable Sensors and Systems (FLEPS). ISSN: 2832-8256. June 2024, pp. 1–4. DOI: 10.1109/FLEPS61194.2024.10603569.